

Reduction of capacitive coupling in inductively coupled plasmas by solenoid coils on dielectric window

Cite as: J. Appl. Phys. **126**, 123302 (2019); <https://doi.org/10.1063/1.5116585>

Submitted: 25 June 2019 . Accepted: 05 September 2019 . Published Online: 25 September 2019

Bocong Zheng , Maheshwar Shrestha, Keliang Wang, Thomas Schuelke , Evgeny Shun'ko, Veniamin Belkin, and Qi Hua Fan 



[View Online](#)



[Export Citation](#)



[CrossMark](#)

ARTICLES YOU MAY BE INTERESTED IN

[Probing changes in secondary electron yield from copper electrodes due to surface defects and changes in crystal orientation](#)

Journal of Applied Physics **126**, 123301 (2019); <https://doi.org/10.1063/1.5113642>

[Effects of the extraction voltage on the beam divergence for a H⁻ ion source](#)

Journal of Applied Physics **126**, 123303 (2019); <https://doi.org/10.1063/1.5116413>

[Terahertz field confinement and enhancement in various sub-wavelength structures](#)

Journal of Applied Physics **126**, 120901 (2019); <https://doi.org/10.1063/1.5110046>

Lock-in Amplifiers

[Find out more today](#)



Zurich
Instruments

Reduction of capacitive coupling in inductively coupled plasmas by solenoid coils on dielectric window

Cite as: J. Appl. Phys. 126, 123302 (2019); doi: 10.1063/1.5116585

Submitted: 25 June 2019 · Accepted: 5 September 2019 ·

Published Online: 25 September 2019



View Online



Export Citation



CrossMark

Bocong Zheng,¹ Maheshwar Shrestha,^{1,2} Keliang Wang,¹ Thomas Schuelke,^{1,3} Evgeny Shun'ko,⁴ Veniamin Belkin,⁴ and Qi Hua Fan^{1,3,5,a)}

AFFILIATIONS

¹Fraunhofer Center for Coatings and Diamond Technologies, Michigan State University, East Lansing, Michigan 48824, USA

²Scion Plasma LLC, Okemos, Michigan 48864, USA

³Department of Electrical and Computer Engineering, Michigan State University, East Lansing, Michigan 48824, USA

⁴Ampres, Inc., 3939 Bestech Dr. Suite D, Ypsilanti, Michigan 48197, USA

⁵Department of Chemical Engineering and Materials Science, Michigan State University, East Lansing, Michigan 48824, USA

^{a)}Author to whom correspondence should be addressed: qfan@egr.msu.edu

ABSTRACT

Solenoid coils with grounded ends positioned on the dielectric window were proposed and numerically studied to reduce the capacitive coupling in conventional inductively coupled plasma (ICP) sources. The capacitive coupling between the plasma and the coils was subsequently suppressed, leading to a significant reduction of the window erosion. To understand the plasma characteristics and the advantages of this configuration, the discharges by the solenoid coil were modeled and compared with a conventional planar coil ICP discharge. The solenoid coil could generate a plasma with higher density than the planar coil under the same absorbed power. The ratio of inductive to capacitive heating power of the solenoid coil was more than one magnitude higher than that of the planar ICP source. The voltage drop on the dielectric window under the solenoid coil was significantly reduced, which was attributed to a potential shielding effect of the grounded end of the radio frequency coil.

Published under license by AIP Publishing. <https://doi.org/10.1063/1.5116585>

I. INTRODUCTION

Inductively coupled plasmas (ICPs) are extensively used for etching and depositing various thin films.^{1–4} ICP sources offer several advantages over other plasma sources, including a high plasma density up to $10^{11–12}/\text{cm}^3$ under low working pressures, a controllable ion flux and energy, and a simple configuration.^{5,6}

It is well known that there are two distinct modes in the ICP discharges: the electrostatic E-mode with low-density plasmas primarily excited by the capacitive coupling of radio frequency (RF) power from the induction coil to the plasma and the electromagnetic H-mode with high-density plasmas predominantly excited by the inductive coupling. Increasing the applied power or the RF current in the coil can trigger a transition from E-mode to H-mode, at which the plasma density increases rapidly.^{7–16} However, even in the H-mode, the plasma is always to some extent generated by the

capacitive coupling component. The capacitive coupling between the dielectric window contacting the RF coil and the excited plasmas may cause considerable sputtering, resulting in severe erosion of the dielectric window and subsequently the plasma contamination.¹⁷ At the end of the last century, several methods have been developed to suppress the capacitive coupling, such as adding a Faraday shield,¹⁸ modifying the dielectric window shape,¹⁹ or applying an axial magnetic field.²⁰ New methods have been proposed in the last two decades. Recent experimental progresses for suppressing capacitive coupling in ICP include using a multicusp magnetic field,²¹ parallel resonance antenna,²² low-inductance antenna units,²³ as well as terminal capacitors.^{24–28}

In this paper, we proposed a solenoid antenna structure that does not share the limitations of conventional ICP sources. By positioning the grounded ends on the dielectric window, the capacitive

coupling between the plasma and the coils was subsequently suppressed, leading to a significant reduction of the dielectric window erosion as well as the plasma contamination. In addition, this configuration has great potential for further development. For example, by combining two induction coils wound in opposite directions, the RF coil current I_{coil} required to ignite and maintain the discharge can be further reduced, due to the induced electric field being weakened. The coil voltage V_{coil} is expected to be reduced as well since $V_{\text{coil}} \propto I_{\text{coil}}$. However, even without further development, the simple solenoid antenna structure with grounded ends on the dielectric window has been able to significantly reduce the capacitive coupling in ICP discharges, leading to multiple benefits for thin film deposition processes, such as reduced plasma contamination, higher growth rates, and superior quality of deposited thin films.

This paper is organized as follows. In Sec. II, the model geometry of the solenoid coil is discussed, the electromagnetic module used for solving the inductive and the capacitive field components and the plasma fluid module used for solving the plasma parameters are described. In Sec. III, the calculated electron density and temperature, the capacitively and inductively coupled powers, as well as the voltage drops on the dielectric window at various absorbed powers are presented. Finally, the conclusions are given in Sec. IV.

II. MODEL DESCRIPTION

The schematic diagram of the solenoid coil is illustrated in Fig. 1. RF power is connected to the upper left corner of the coil. The grounded ends of this coil are positioned above a dielectric window on the outside of a vacuum chamber. Since the lowest turn is at the ground potential, the RF potential increases in the coil away from this end. Hence, the solenoid coil is expected to have negligible capacitive coupling with the excited plasma, as will be shown later. The voltage drop on the window surface is therefore reduced, as well as the window erosion and the plasma contamination.

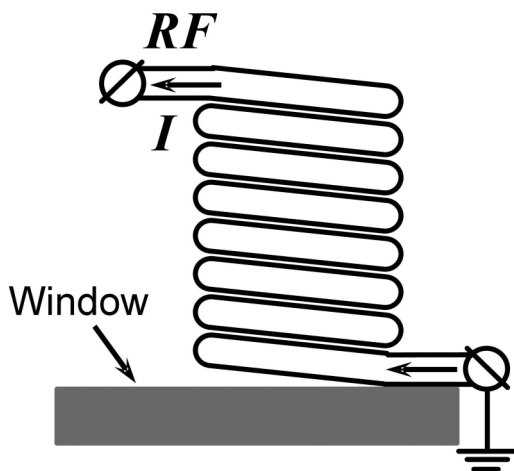


FIG. 1. Schematic diagram of the solenoid coil.

The ICP discharges by one solenoid coil are modeled and compared with the planar coil discharges in an axisymmetric coordinate as demonstrated in Fig. 2. The radius of the cylindrical ICP discharge chamber is 5 cm, including the vacuum vessel, the dielectric window and the reaction chamber. For the solenoid coil illustrated in Fig. 2(a), a ten-turn solenoid coil is placed in vacuum, 1.5 mm above the 7 mm thick dielectric window. The coil radius is 7 mm, the coil wire diameter is 3 mm, and the spacing between the coil wires is 0.5 mm. The lowest coil above the window is grounded, and the highest coil is connected to the RF source. For the planar coil illustrated in Fig. 2(b), a four-turn planar coil is used instead of the solenoid coil. The innermost radius is 7 mm, and the spacing between coils is 7.5 mm. One end of the outermost coil is grounded, and one end of the innermost coil is connected to the RF source. Both the solenoid and the planar coils are powered with a 13.56 MHz RF current source. The RF current in the coils induces an azimuthal electric field, inductively heating the electrons in the H-mode. The voltage drop across the end of RF source and the grounded coil induces radial and axial electric fields, capacitively heating the electrons in the E-mode. The working gas is Ar and the working pressure is set as 50 mTorr for all the calculations in this study. The model includes an electromagnetic module and a plasma fluid module, which are described below.

At the high driving frequency of 13.56 MHz used in the model, the ion motion can be neglected in the electromagnetic module, and the plasma parameters can be assumed as invariable during the calculation of the electromagnetic field profiles. By assuming a time variation in the form of $\exp(-i\omega t)$, Maxwell's

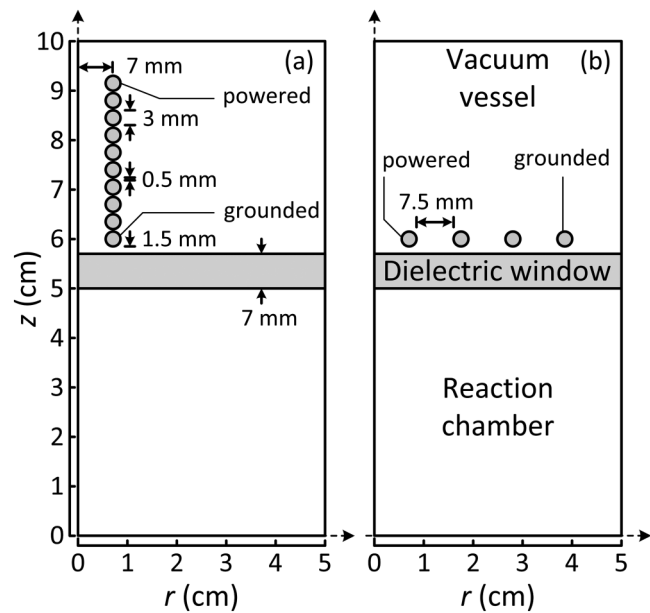


FIG. 2. Schematic diagram of the simulation region of (a) the solenoid coil and (b) the planar coil.

equations can be written as

$$\begin{aligned}\nabla \times \mathbf{E} &= i\omega \mathbf{B}, \\ \nabla \times \mathbf{B} &= \mu_0 \mathbf{J} - i\omega \epsilon \mu_0 \mathbf{E},\end{aligned}\quad (1)$$

where \mathbf{E} and \mathbf{B} are the RF electric and magnetic field vectors, ω is the angular frequency of the RF power source, ϵ_0 and μ_0 are the permittivity and permeability of free-space, the absolute permittivity $\epsilon = \kappa_r \epsilon_0$ depends on the relative dielectric constant κ_r . $\mathbf{J} = \mathbf{J}_{\text{coil}} + \mathbf{J}_{\text{ind}}$ is the current density that includes the RF current in the coil \mathbf{J}_{coil} and the induced current $\mathbf{J}_{\text{ind}} = \sigma_p \mathbf{E}$, where σ_p is the electrical conductivity of the plasma. According to the Maxwell's equations, the RF electric field satisfies^{29,30}

$$\nabla \times \nabla \times \mathbf{E} - \frac{\omega^2}{c^2} \kappa_r \mathbf{E} = i\omega \mu_0 \mathbf{J}_{\text{coil}}, \quad (2)$$

where c is the speed of light in vacuum. Since \mathbf{J}_{coil} only has an azimuthal component J_θ , Eq. (2) is reduced to

$$\nabla^2 E_\theta + \frac{\omega^2}{c^2} \kappa_r E_\theta = -i\omega \mu_0 J_\theta, \quad (3)$$

from where the azimuthal electric field is obtained. The radial and axial components of the electric field $(E_r, E_z) = -\nabla \Phi$ are obtained from^{29,30}

$$\nabla \cdot (\kappa_r \nabla \Phi) = 0. \quad (4)$$

The coil voltage can be estimated as^{31,14}

$$V_{\text{coil}} = I_{\text{coil}} |Z_H|, \quad (5)$$

where $Z_H = R_H + i\omega L_H$, R_H is the sum of the coil resistance R_{coil} and the plasma resistance R_p , while L_H equals to the coil inductance L_{coil} minus the plasma inductance L_p , since that the plasma inductance always counteracts the coil inductance,

$$\begin{aligned}R_H &= R_{\text{coil}} + R_p, \\ L_H &= L_{\text{coil}} - L_p.\end{aligned}\quad (6)$$

The plasma resistance R_p could be solved from

$$P_p = \frac{1}{2} I_{\text{coil}}^2 R_p, \quad (7)$$

where P_p equals to the surface integral of the Poynting vector along the dielectric window A_d ,

$$P_p = \frac{1}{2\mu_0} \text{Re} \left(\int_{A_d} E_\theta(r, z_0) B_r^*(r, z_0) dA \right), \quad (8)$$

where $z_0 = 5.7$ cm is the height position of the window. Similarly,

the plasma inductance can be expressed as^{31,32}

$$\begin{aligned}L_p &= \frac{2}{\omega I_{\text{coil}}^2} \left[\frac{1}{2\mu_0} \text{Im} \left(\int_{A_d} (E_{\theta_v}(r, z_0) B_{r_v}^*(r, z_0) - E_\theta(r, z_0) B_r^*(r, z_0)) dA \right) \right. \\ &\quad \left. + \frac{\omega}{v_m} \frac{1}{2\mu_0} \text{Re} \left(\int_{A_d} E_\theta(r, z_0) B_r^*(r, z_0) dA \right) \right],\end{aligned}\quad (9)$$

where E_{θ_v} and B_{r_v} are the electric and magnetic fields in the vacuum chamber without a plasma. The estimated coil voltage V_{coil} is set as the boundary condition at the powered end of the coils. The boundary conditions on the other turns are obtained by assuming the electric potential drops linearly along the azimuthal direction. The resistances of the solenoid and the planar coils used in the model are 0.1 and 0.068 Ω and the corresponding inductances are 0.47 and 0.72 μH, respectively. The relative dielectric constants for the materials used in the simulation are shown in Table I. The boundary condition for the magnetic potential A at the chamber walls is $A = 0$. For the grounded chamber walls, the boundary condition is $\Phi = 0$. At the left boundary at $r = 0$ cm, the boundary condition is axisymmetric.

The time-averaged Ohmic heating power deposition in the plasma, including the capacitively and the inductively coupled components, is^{13,33}

$$\begin{aligned}P_{\text{dep}}(r, z) &= P_{\text{ind}}(r, z) + P_{\text{cap}}(r, z) \\ &= \underbrace{\frac{1}{2} \text{Re}(\sigma_p |E_\theta(r, z)|^2)}_{\text{inductive}} + \underbrace{\frac{1}{2} \text{Re}(\sigma_p |E_r(r, z)|^2)}_{\text{capacitive}} + \underbrace{\frac{1}{2} \text{Re}(\sigma_p |E_z(r, z)|^2)}_{\text{capacitive}}.\end{aligned}\quad (10)$$

For the argon plasma used in the simulation, the species considered are electrons e, argon ions Ar^+ , and argon metastables Ar^m . The mass and energy balance of electrons in the bulk plasma is governed by the continuity and the energy conservation equations,

$$\begin{aligned}\frac{\partial n_e}{\partial t} + \nabla \cdot \Gamma_e &= R_e, \\ \frac{\partial}{\partial t} \left(\frac{3}{2} n_e T_e \right) + \nabla \cdot \mathbf{q}_e + \mathbf{E}_s \cdot \Gamma_e &= Q + P_{\text{dep}}.\end{aligned}\quad (11)$$

The drift-diffusion flux of electrons is $\Gamma_e = -\mu_e n_e \mathbf{E}_s - \nabla(D_e n_e)$, where \mathbf{E}_s is the electrostatic field, $\mu_e = \frac{e}{m_e V_m}$ is the electron mobility, and $D_e = \mu_e T_e$ is the diffusion coefficient of electrons calculated from Einstein's relationship, and T_e is the electron temperature. $v_m = \sum_j k_j n_j$ is the collision frequency of electrons, where k_j is the rate coefficient of electron collisions with species j . $R_e = \sum_j k_{e,j} n_j n_e$

TABLE I. Electromagnetic properties of materials used in the model.

| | Air | Dielectric | Copper |
|------------|-----|------------|---------------------|
| σ | 0 | 0 | 6×10^7 S/m |
| κ_r | 1 | 4.5 | 1 |

is the ionization rate, where k_{izj} is the ionization rate coefficient of electron collisions with species j , n_j is the number density of species j . In the energy conservation equation of electrons, the source term of electron energy is the Ohmic heating from the inductive and capacitive fields, P_{dep} , the sink terms are collisional energy losses, $Q = \sum_j k_j n_j n_e \Delta \epsilon_j$, due to polarization scattering and inelastic collisions, and the Joule heating from the ambipolar field, $\mathbf{E}_s \cdot \boldsymbol{\Gamma}_e$. $\Delta \epsilon_j$ is the energy variation of elastic and inelastic collisions between electron and species j , and $\mathbf{q}_e = \frac{5}{2} T_e \boldsymbol{\Gamma}_e - \frac{5}{2} n_e D_e \nabla T_e$ is the electron energy flux.

Similar to the electrons, the continuity equations of heavy species α can be derived as

$$\frac{\partial n_\alpha}{\partial t} + \nabla \cdot \boldsymbol{\Gamma}_\alpha = R_\alpha, \quad (12)$$

where $\alpha = \text{Ar}^m, \text{Ar}^+$, n_α and $\boldsymbol{\Gamma}_\alpha = z_\alpha \mu_\alpha n_\alpha \mathbf{E}_s - \nabla(D_\alpha n_\alpha)$ are the number density and the diffusion flux of α , where z is the charge number and R_α is the rate expression for species α . The Ar ion mobility depends on the electrostatic field \mathbf{E}_s and is coming from the experimental measurements.^{34,35} The corresponding diffusion coefficient for Ar^+ is calculated from Einstein's relation.

The electrostatic field and potential can be obtained by solving Poisson's equation. The rate coefficients used in the model are shown in Table II. The electron energy distribution function (EEDF) is assumed as Maxwellian for the rate coefficients.

The boundary conditions for the electron mass and energy fluxes are

$$\Gamma_e = \frac{1}{4} n_e \sqrt{8T_e/\pi m_e} \quad (13)$$

and

$$\mathbf{q}_e = \frac{5}{2} T_e \boldsymbol{\Gamma}_e. \quad (14)$$

The flux of heavy species at the electrodes is calculated as⁴⁰

$$\Gamma_\alpha = \frac{\gamma_\alpha}{1 - \gamma_\alpha/2} \frac{1}{4} n_\alpha \sqrt{\frac{8k_B T_\alpha}{\pi m_\alpha}} + z_\alpha \mu_\alpha E n_\alpha, \quad (15)$$

where $\gamma_\alpha = 1$ is the sticking coefficient, k_B is the Boltzmann constant, and $\sqrt{8k_B T_\alpha / \pi m_\alpha}$ is the averaged thermal velocity of heavy species α .

The RF sheath voltage magnitude, \tilde{V}_s , is estimated by the capacitance divider formula, $\tilde{V}_s = \tilde{V}_d \frac{C_d}{C_s + C_d}$, where \tilde{V}_d is the

voltage drop across the dielectric window and the plasma sheath. $C_d = \frac{\kappa_d \epsilon_0 A_d}{d}$ is the capacitance of the dielectric window, where $\kappa_d = 4.5$ is the relative dielectric constant of the dielectric window as shown in Table I, $d = 7$ mm is the window thickness. $C_s = 0.61 \frac{\epsilon_0 A_d}{s_m}$ is the sheath capacitance,⁵ where s_m is the time-averaged sheath thickness. s_m depends on the DC sheath voltage \bar{V}_s and can be derived from the ion current

$$\bar{J}_i = 0.82 \epsilon_0 \left(\frac{2e}{M_i} \right)^{1/2} \frac{\bar{V}_s^{3/2}}{s_m^2}, \quad (16)$$

where the DC sheath voltage is estimated as $\bar{V}_s \approx 0.83 \tilde{V}_s + |\Phi_w|$.⁵ The floating potential Φ_w is added to ensure a minimum sheath thickness when $\tilde{V}_s = 0$ V. From the ion current at the wall, $\bar{J}_i = e n_w u_w$, where n_w and u_w are the ion density and velocity at the wall, and the ion energy conservation in the sheath, $\frac{1}{2} M_i u_w^2 = \frac{1}{2} M_i u_B^2 + e \bar{V}_s$, where u_B is the Bohm velocity, we have

$$s_m = \left(\frac{0.82 \epsilon_0}{e n_w} \right)^{1/2} \frac{\bar{V}_s^{3/4}}{\left(\frac{T_e}{2} + \bar{V}_s \right)^{1/4}}. \quad (17)$$

Once \tilde{V}_s is obtained, the stochastic heating flux can be calculated as³³

$$S_{\text{stoc}} = 0.45 \left(\frac{m_e}{e} \right)^{1/2} \epsilon_0 \omega^2 \tilde{V}_s T_e^{1/2}. \quad (18)$$

To include the stochastic heating in the sheath, the boundary condition for the electron energy flux, Eq. (14), is modified as

$$\mathbf{q}_e \cdot \hat{\mathbf{n}} = \frac{5}{2} T_e \boldsymbol{\Gamma}_e \cdot \hat{\mathbf{n}} - S_{\text{stoc}}, \quad (19)$$

where $\hat{\mathbf{n}}$ is the unit vector perpendicular to the plasma-wall boundary. The ion heating flux S_{ion} is the ion current multiplied by the DC sheath voltage,

$$S_{\text{ion}} = \bar{J}_i \bar{V}_s = e \bar{V}_s n_w u_w. \quad (20)$$

III. RESULTS AND DISCUSSION

Using the model described in Sec. II, the plasma discharge processes of the solenoid and the planar coils were calculated at various absorbed powers. The electron density, electron temperature, and the power depositions were studied. In addition, the voltage drop on the dielectric window was examined.

TABLE II. Principal rate coefficients for the Ar plasma.

| Reaction | Rate coefficient (m^3/s) | Threshold (eV) | Reference |
|--|---|----------------|-----------|
| $e + \text{Ar} \rightarrow e + \text{Ar}$ | $2.336 \times 10^{-14} T_e^{1.609} \times \exp(0.0618(\ln T_e)^2 - 0.1171 (\ln T_e)^3)$ | | 5 |
| $e + \text{Ar} \rightarrow 2e + \text{Ar}^+$ | $2.34 \times 10^{-14} T_e^{0.59} \exp(-17.44/T_e)$ | 15.76 | 36 |
| $e + \text{Ar} \rightarrow e + \text{Ar}^m$ | $2.5 \times 10^{-15} T_e^{0.74} \exp(-11.56/T_e)$ | 11.56 | 37 |
| $e + \text{Ar}^m \rightarrow e + \text{Ar}$ | $4.3 \times 10^{-16} T_e^{0.74}$ | -11.56 | 38 |
| $e + \text{Ar}^m \rightarrow 2e + \text{Ar}^+$ | $6.8 \times 10^{-15} T_e^{0.67} \exp(-4.2/T_e)$ | 4.2 | 39 |

Assuming equal electron and ion fluxes to the wall, the power lost by the electrons and by the ions are different, depending on the mean kinetic energy lost per particle lost.⁵ The power lost by the electrons has been considered in the boundary conditions of Eq. (11). However, the total power absorbed by the plasma considered here equals the overall discharge energy losses, which depends on the collisional energy losses, the kinetic energy carried by electrons, and ions to the walls. The outer boundaries for the plasma fluid equations in this model are not the chamber walls but the plasma-sheath boundaries. The ions entering the sheath are further accelerated in the sheath electric field, which is not considered in the electron energy balance equation. Therefore, the absorbed power P_{abs} includes both bulk Ohmic heating and sheath heating and is defined as

$$\begin{aligned} P_{\text{abs}} &= P_{\text{bulk}} + P_{\text{sh}} \\ &= P_{\text{Cap}} + P_{\text{Ind}} + P_{\text{stoc}} + P_{\text{ion}} \\ &= \int_{V_p} (P_{\text{cap}} + P_{\text{ind}}) dV + \int_{A_s} (S_{\text{stoc}} + S_{\text{ion}}) dA, \end{aligned} \quad (21)$$

where P_{Cap} and P_{Ind} are the power absorbed by capacitively and inductively Ohmic heatings in the plasma reaction chamber V_p , P_{stoc} , and P_{ion} are the power absorbed by the stochastic heating and the power delivered to the ions by falling through the DC sheath potential, respectively, and A_s is the sheath area. The coil current is adjusted to achieve the desired P_{abs} in the simulation. The calculated spatial distributions of the electron density are illustrated in Fig. 3. The spatial distributions of n_e are essentially unchanged. Both the solenoid and the planar coils are operated in the E-mode at low absorbed powers of 0.1 W and in the H-mode at 15 W. However, the maximal electron densities of the solenoid coil are always higher than that of the planar coil, and the difference gradually increases as the power goes up. The lower plasma density for the planar coil can be attributed to its higher power of P_{ion} that is

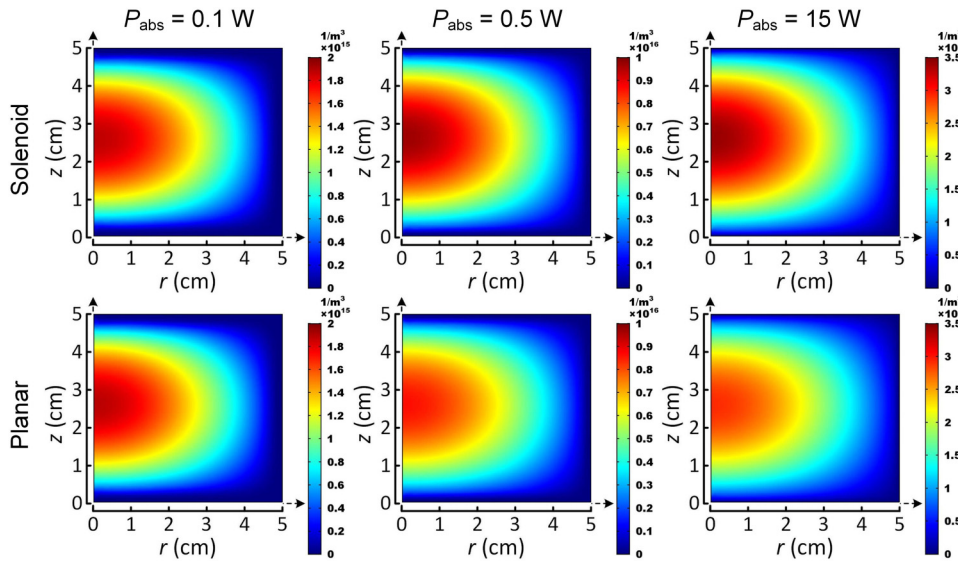


FIG. 3. The spatial distributions of the electron density n_e for solenoid and planar coils at various absorbed powers of 0.1 W, 0.5 W, and 15 W.

proportional to the absorbed power P_{abs} , since the P_{ion} is lost on the dielectric window and the chamber wall, and does not contribute to the plasma generation. For both the solenoid and the planar coils, the ratio of $P_{\text{ion}}/P_{\text{abs}}$ is about 23% and the maximal electron density is $1.9 \times 10^{15}/\text{m}^3$ at $P_{\text{abs}} = 0.1$ W. As P_{abs} increases to 15 W, the ratio decreases slightly to 21% for the solenoid coil but increases significantly to 30% for the planar coil, the obtained electron densities are about $3.5 \times 10^{17}/\text{m}^3$ and less than $3 \times 10^{17}/\text{m}^3$, respectively. The reason the solenoid coil can maintain a low ratio of $P_{\text{ion}}/P_{\text{abs}}$ is that it reduces the voltage drop on the dielectric window, which will be discussed later.

The distributions of capacitive power deposition by Ohmic heating are demonstrated in Fig. 4. The power density is expressed in logarithm form to illustrate the distribution details more clearly. High power densities can be observed near the boundary, especially on the dielectric window, due to the high capacitive electric field induced by the high voltage terminal of the RF source. The thin layer near the grounded walls is derived from the sheath heating caused by the radial and axial electric field near the walls. Similar profiles of P_{cap} have been observed in other works.³³ For the solenoid coil, P_{cap} is significantly reduced in the H-mode at 15 W. On the contrary, the planar coil still has a relatively high capacitive power density. The inductive power deposition by Ohmic heating are calculated as well, as shown in Fig. 5. The distribution form of P_{ind} is opposite to P_{cap} , that the highest power density appears in the bulk plasma, which is consistent with the inductive electric field E_θ . P_{ind} of the solenoid coil is higher than the planar coil under all absorbed powers.

Contrary to the distribution of the electron density, both the magnitude and the distribution of the electron temperature T_e depend on the absorbed power, as illustrated in Fig. 6. As P_{abs} increases from 0.1 to 15 W, T_e maximum decreases from about 3.3 V (solenoid) and 4.2 V (planar) in the E-mode to about 2.4 V in the H-mode, and the distribution becomes more uniform. These phenomena have been attributed to the variation of the capacitive

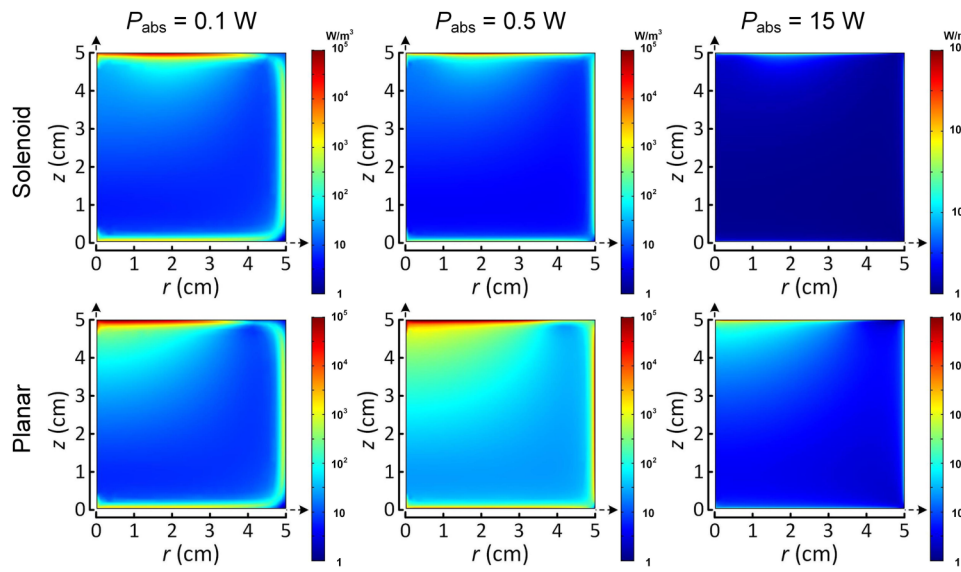


FIG. 4. The capacitive component distributions of Ohmic heating P_{cap} for solenoid and planar coils at various absorbed powers of 0.1 W, 0.5 W, and 15 W.

and inductive electromagnetic fields at different discharge modes.¹³ For the solenoid coil discharges, the maximums of E_z and E_θ appear around $r = 1\text{--}2\text{ cm}$ under the dielectric window (data not shown); therefore, the position of T_e maximum has no significant change with increasing power. However, for the planar coil discharges, as increasing the power, the position of T_e maximum moves away from the center. This is because the maximum of E_z appears under the powered end of the planar coil, which is near the center, and the maximum E_θ appears at the middle position of the coil. Therefore, the maximum T_e in the planar coil discharge moves away from the center as the discharge transforms from the low-density E-mode to the high-density H-mode.

The more detailed power fractions under different absorbed powers are illustrated in Fig. 7. The absorbed power ranges from 0.01 to 100 W and is represented in logarithmic coordinates. From Fig. 7(a), it can be seen that at the lowest absorbed power of 0.01 W, the solenoid coil discharge is maintained by the pure E-mode, $P_{\text{Cap}} + P_{\text{stoc}} + P_{\text{ion}}$, the inductive coupling of P_{Ind} can be neglected. The capacitive Ohmic heating power P_{Cap} occupies the largest fraction of the absorbed power, up to 40%. The second is the stochastic heating P_{stoc} , about 35%, and the remaining part is the capacitive power delivered to the ions. The fraction of stochastic heating keeps decreasing as the absorbed power goes up, since its absolute value changes little. The fraction of P_{ion} remains

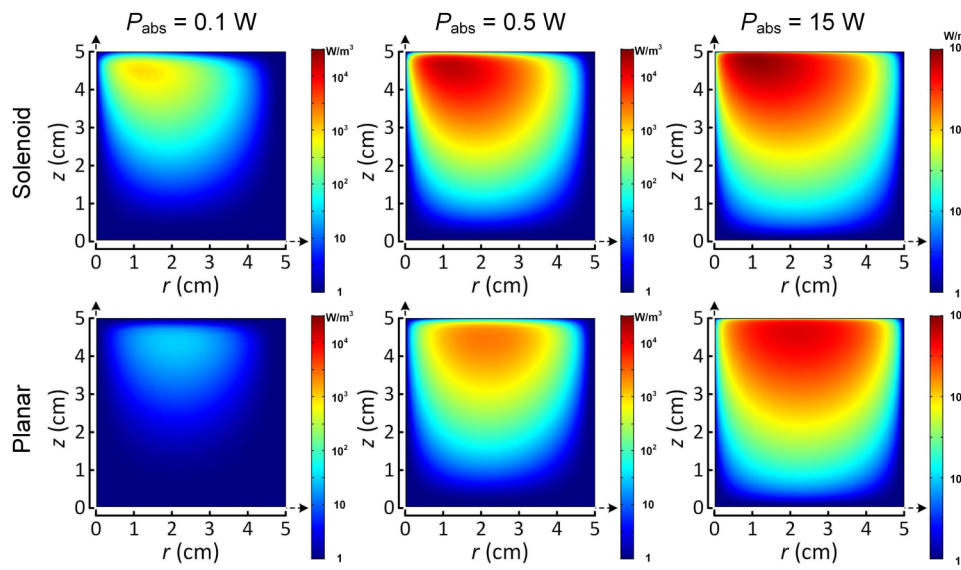


FIG. 5. The inductive component distributions of Ohmic heating P_{ind} for solenoid and planar coils at various absorbed powers of 0.1 W, 0.5 W, and 15 W.

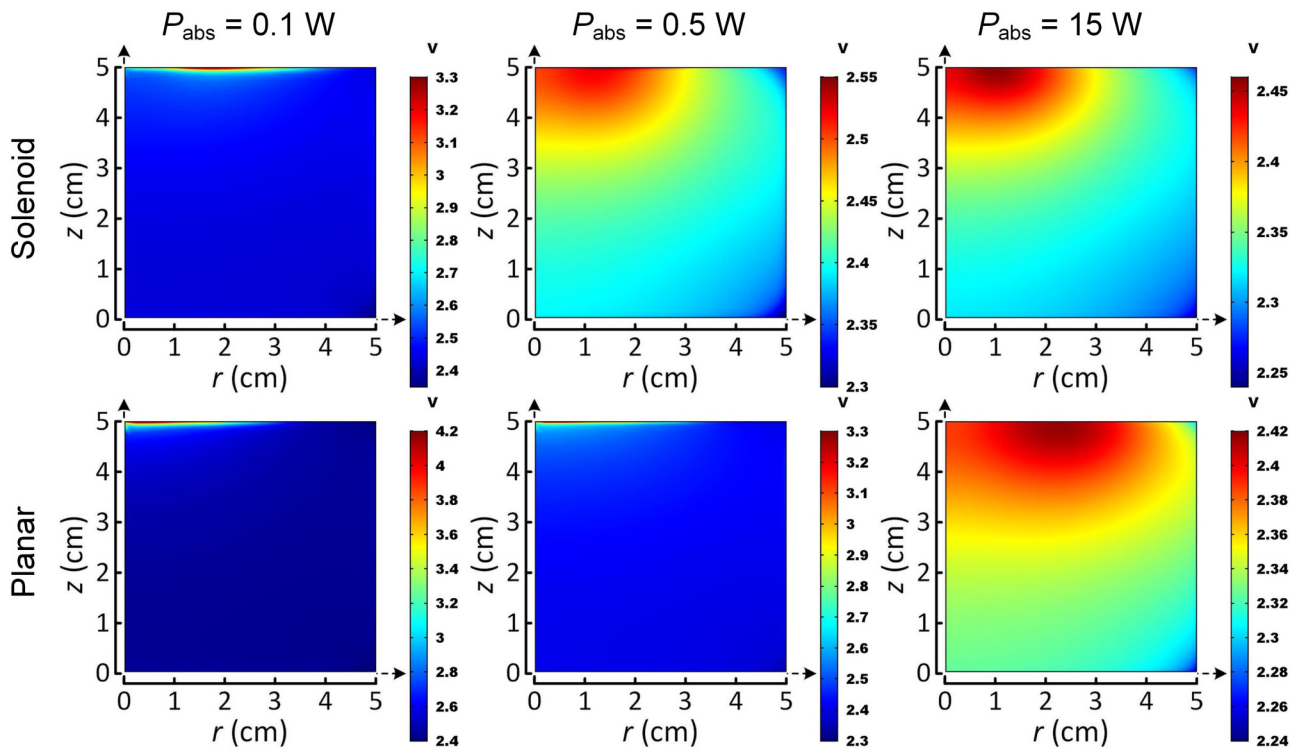


FIG. 6. The spatial distributions of the electron temperature T_e for solenoid and planar coils at various absorbed powers of 0.1 W, 0.5 W, and 15 W.

slightly above 20% under all powers. The fraction of P_{Cap} shows a dramatic decrease from 0.1 to around 1 W, correspondingly, the fraction of P_{Ind} increases rapidly, indicating an E to H transition. The variation of the power fractions of the planar coil illustrated in Fig. 7(b) is similar to Fig. 7(a). However, the fraction of the inductive coupling is always lower than the solenoid coil. In addition, P_{ion} increases from about 20% at 0.01 W to more than 30% at 1 W and remains until 100 W. This is also the reason the planar coil has a lower electron density under the same absorbed power. Comparing Figs. 7(a) and 7(b), the transition regime between 0.1 W and 1 W is sharper for the planar coil. This can explain the difference in the distribution characteristics of T_e at 0.5 W in Fig. 6, since the maximum electron temperature is higher and the distribution is less uniform in the E-mode. Furthermore, in inductive mode both discharges show almost the same fraction of inductive coupling. The ratio of P_{Ind} to P_{abs} at various absorbed powers is given in Fig. 7(c). The inductive coupling power P_{Ind} is always more than one magnitude higher than P_{Cap} , implying that the configuration of solenoid coil can effectively reduce the capacitive coupling.

The DC sheath voltage \bar{V}_s on the dielectric window is shown in Fig. 8. For the planar coil, as seen in Fig. 8(a), three peaks appear along the radial position, corresponding to the three coils on the left above the window. The fourth turn of coil is grounded so there is no peak. Nonintuitively, although the inductive coupling

is more efficient at higher powers, the sheath voltage of the planar coil increases with the increase of P_{abs} . This is due to the increase in voltage drop \bar{V}_d across the dielectric window and the plasma sheath, which in turn is caused by an increase in the voltage of the powered coil end, from about 60 V to nearly 500 V as the power increases from 0.1 W to 15 W. The sheath voltage only increases slightly when the power varies from 0.5 to 15 W. This is because the increase of the coil voltage is offset by the reduction of sheath thickness at higher plasma densities, i.e., the portion of voltage drop in the sheath is decreased. The highest voltage appears below the powered end at $r = 7$ mm, up to 100 V at 15 W. This has exceeded the sputtering energy threshold of the dielectric materials and can result in severe window erosion and plasma contamination. For the solenoid coil, as shown in Fig. 8(b), the maximal \bar{V}_s appears at around $r = 1.5$ cm under all the absorbed powers. The local minimums around $r = 7$ mm are caused by the potential shielding of the grounded end located here. As the absorbed power increases from 0.1 to 15 W, the maximal \bar{V}_s in the solenoid coil discharge decreases from 28 to 18 V, even below the sputtering energy threshold of the dielectric window.^{41,42} This should be attributed to the reduced sheath thickness, while the voltage drop \bar{V}_d is restricted by the grounded end. The above calculations demonstrate that this configuration can significantly suppress the voltage drop on the dielectric window, thus prolonging the service life of the dielectric window and obtaining contamination-free plasmas.

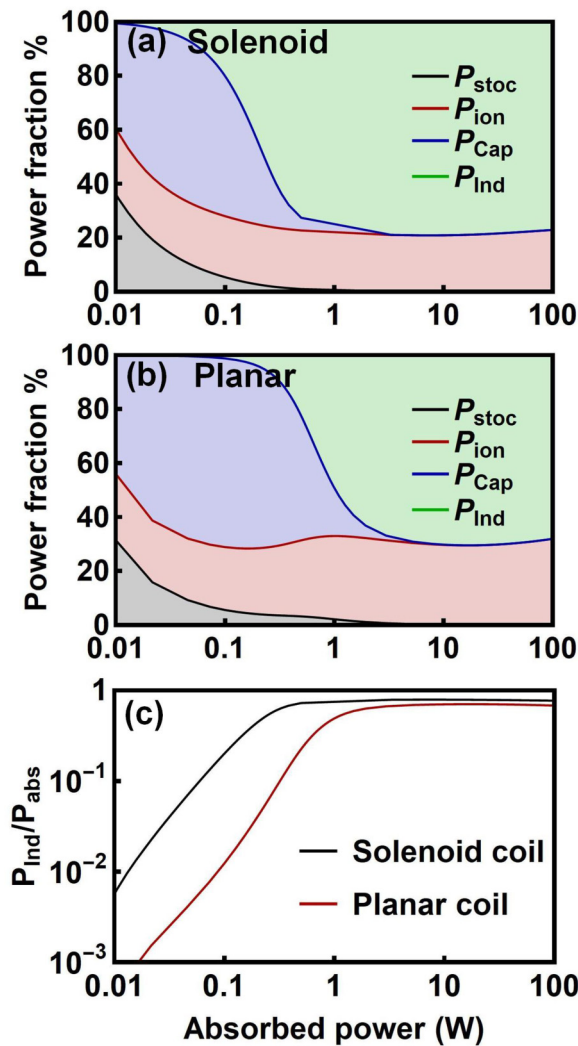


FIG. 7. (a) The power fractions of the solenoid coils, (b) the power fractions of the planar coils, and (c) the $P_{\text{Ind}}/P_{\text{abs}}$ ratio vs the absorbed power P_{abs} .

To validate the present model, we benchmarked the model with the experimental data of Godyak *et al.*⁴³ The geometry and input parameters used for benchmark are the same as the experiment. The inner radius of the chamber is 9.9 cm and the length is 10.5 cm, and the RF source frequency is 6.78 MHz. Figure 9 presents the experimental data from Ref. 43 and the corresponding model results. There is good agreement between the model results and the experimental data, indicating the validity of the model.

An experimental setup with two induction coils has been successfully tested, as shown in Fig. 10. Experimentally, the ignition for the configuration of one solenoid coil on the dielectric window is not very easy and requires a relatively large current. However, by combining two induction coils wound in opposite directions and positioning the grounded ends on the dielectric window, as shown

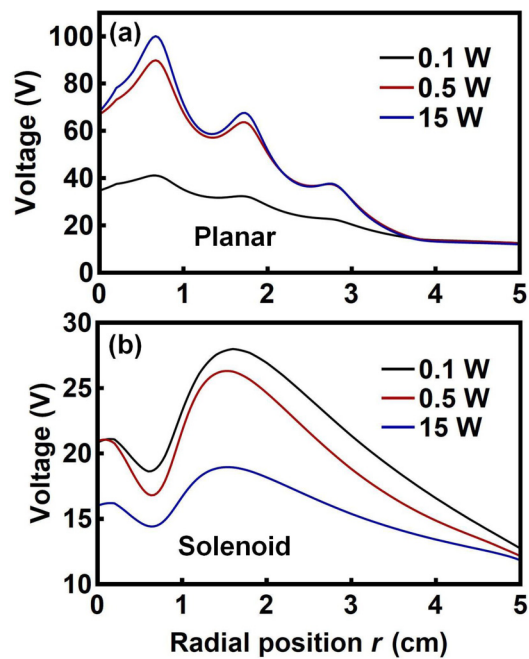


FIG. 8. The DC sheath voltage \bar{V}_s on the dielectric window of (a) the solenoid coil and (b) the planar coil at various absorbed powers of 0.1 W, 0.5 W, and 15 W.

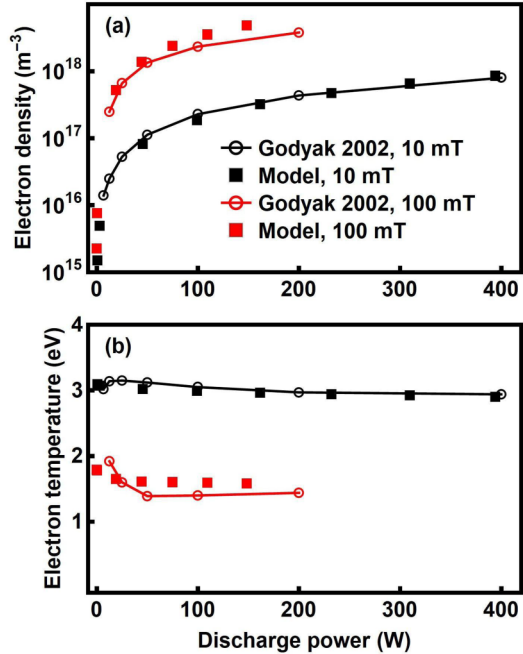


FIG. 9. Model results and experimental data from Godyak *et al.*⁴³ for 10 and 100 mTorr argon discharges, showing (a) electron density and (b) electron temperature.

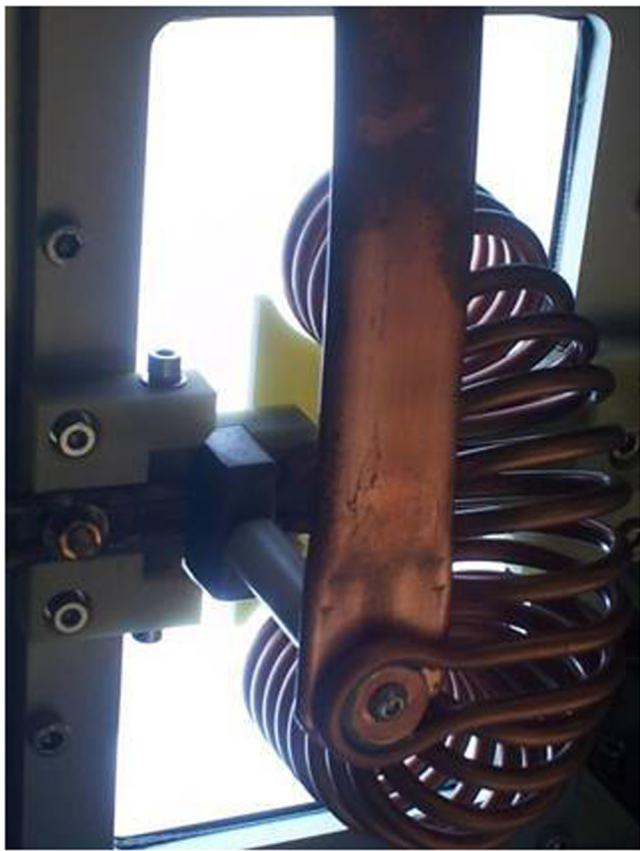


FIG. 10. An experimental setup with two induction coils wound in opposite directions and positioning the grounded ends on the dielectric window.

in Fig. 10, the discharge can be easily ignited, since the electromagnetic fields generated by the symmetrical solenoid coils are mutually enhanced. In this work, one solenoid coil on the dielectric window was selected as the modeling object, due to the following reasons. First, the simplified geometry facilitates the comparison with the planar coil configuration. Secondly, the discharge induced by one solenoid coil can be described by a two-dimensional axisymmetric coordinate, instead of the time-consuming three-dimensional simulations. As mentioned above, physically, this simplified solenoid antenna structure requires a higher RF coil current I_{coil} to ignite and maintain the discharge than the symmetrical solenoid coils, as well as the coil voltage V_{coil} , since $V_{\text{coil}} \propto I_{\text{coil}}$. However, a significant reduction of the capacitive coupling can be obtained even at the overestimated coil voltage. Therefore, we point out here that the configuration of a solenoid coil on the dielectric window is both physically and experimentally feasible, this configuration has great potential for further development.

Finally, we briefly discuss the influence of coil configuration on the skin depth and the power coupling. As shown in Fig. 5, for both the solenoid and the planar configuration, the plasma density increases with the absorbed power, leading to a reduction of several

millimeters of the skin layer. By comparing these two configurations, the minimum skin layer of the solenoid configuration is slightly narrower and not as uniform as the planar configuration along the radial direction. Using the transformer model³¹ and adopting the calculated results in our model, the coupling constant k for solenoid configuration at $P_{\text{abs}} = 15$ W is about 0.047, much lower than the planar configuration of about 0.2. However, further analysis reveals that the reduction of k in the solenoid configuration is caused by the higher I_{coil} (about 50 A for solenoid configuration and about 8 A for planar configuration), which can be significantly reduced by adopting the symmetrical solenoid coils as mentioned above. Since the configuration of a single solenoid coil has no advantage in terms of power coupling efficiency, the aim of this study is only to demonstrate the advantage of the solenoid coil configuration in reducing the negative potential on the surface of the insulator window, a detailed analysis of the power coupling may have exceeded the scope of this work. However, an enhancement of the power coupling is expected by adopting the symmetrical solenoid coils configuration demonstrated in Fig. 10. The corresponding analysis requires the simulation of symmetrical solenoid coils, which will be investigated in the future work.

IV. CONCLUSIONS

A two-dimensional plasma fluid model is used to investigate the reduction effect of capacitive coupling in inductively coupled plasma sources by solenoid coils placed on the dielectric window. In comparison with a conventional planar coil ICP discharge, a higher electron density can be achieved at a given absorbed power by the solenoid coil configuration. This is due to the reduction in the fraction of power delivered to the ions, which does not contribute to the plasma generation. The electron temperature distribution depends on the mode of ICP discharges. A nonuniform distribution with a high peak near the dielectric window is observed when the capacitive electric field dominates, while the distribution becomes more uniform and the peak value is significantly reduced when the inductive electric field dominates. The power density of capacitive Ohmic heating peaks near the dielectric window surface, due to the strong capacitive electric field induced by the high voltage terminal of the RF source. The capacitive coupling decreases and the inductive coupling increases as the discharge transforms to the H-mode. The plasma density increases as the absorbed power goes up, leading to a narrower skin layer, and the position of the maximum power deposition of the inductive heating moves toward the coil. With the increase of absorbed power, the ICP discharges by the solenoid coil can transform to the H-mode earlier than the planar coil, since the capacitive coupling is strongly suppressed. By using the solenoid coil instead of the conventional planar ICP source, the ratio of inductive to capacitive power absorbed by the plasma was always more than one magnitude higher at a given absorbed power. A significant reduction of the voltage drop on the dielectric window is also indicated. The voltage drop in the H-mode decreases from up to 100 V to less than 20 V, even below the sputtering energy threshold of the dielectric window. It can be concluded that the use of solenoid coils will greatly suppress the capacitive coupling, reduce the window erosion, as well as prevent the plasma contamination.

ACKNOWLEDGMENTS

This work was partly supported by the National Science Foundation (NSF, Award No. 1700785).

REFERENCES

- ¹M. J. Kushner, W. Z. Collison, M. J. Grapperhaus, J. P. Holland, and M. S. Barnes, "A three-dimensional model for inductively coupled plasma etching reactors: Azimuthal symmetry, coil properties, and comparison to experiments," *J. Appl. Phys.* **80**, 1337–1344 (1996).
- ²T. Ichiki, T. Momose, and T. Yoshida, "Effects of the substrate bias on the formation of cubic boron nitride by inductively coupled plasma enhanced chemical vapor deposition," *J. Appl. Phys.* **75**, 1330–1334 (1994).
- ³L. Delzeit, I. McAninch, B. A. Cruden, D. Hash, B. Chen, J. Han, and M. Meyyappan, "Growth of multiwall carbon nanotubes in an inductively coupled plasma reactor," *J. Appl. Phys.* **91**, 6027–6033 (2002).
- ⁴K. Tao, D. Mao, and J. Hopwood, "Ionized physical vapor deposition of titanium nitride: A global plasma model," *J. Appl. Phys.* **91**, 4040–4048 (2002).
- ⁵M. A. Lieberman and A. J. Lichtenberg, *Principles of Plasma Discharges and Materials Processing* (John Wiley & Sons, 2005).
- ⁶P. Chabert and N. Braithwaite, *Physics of Radio-frequency Plasmas* (Cambridge University Press, New York, 2011).
- ⁷M. M. Turner and M. A. Lieberman, "Hysteresis and the E-to-H transition in radiofrequency inductive discharges," *Plasma Sources Sci. Technol.* **8**, 313–324 (1999).
- ⁸G. Cunge, B. Crowley, D. Vender, and M. M. Turner, "Characterization of the E to H transition in a pulsed inductively coupled plasma discharge with internal coil geometry: Bi-stability and hysteresis," *Plasma Sources Sci. Technol.* **8**, 576–586 (1999).
- ⁹K. Suzuki, K. Nakamura, H. Ohkubo, and H. Sugai, "Power transfer efficiency and mode jump in an inductive rf discharge," *Plasma Sources Sci. Technol.* **7**, 13–20 (1998).
- ¹⁰M.-H. Lee, K. H. Lee, D.-S. Hyun, and C.-W. Chung, "On the hysteresis in E to H and H to E transitions and the multistep ionization in inductively coupled plasma," *Appl. Phys. Lett.* **90**, 191502 (2007).
- ¹¹A. M. Daltrini, S. A. Moshkalev, M. J. R. Monteiro, E. Besseler, A. Kostryukov, and M. Machida, "Mode transitions and hysteresis in inductively coupled plasmas," *J. Appl. Phys.* **101**, 073309 (2007).
- ¹²A. M. Daltrini, S. A. Moshkalev, T. J. Morgan, R. B. Piejak, and W. G. Graham, "Plasma power measurement and hysteresis in the E-H transition of a rf inductively coupled plasma system," *Appl. Phys. Lett.* **92**, 061504 (2008).
- ¹³S.-X. Zhao, X. Xu, X.-C. Li, and Y.-N. Wang, "Fluid simulation of the E-H mode transition in inductively coupled plasma," *J. Appl. Phys.* **105**, 083306 (2009).
- ¹⁴H.-J. Xu, S.-X. Zhao, Y.-R. Zhang, F. Gao, X.-C. Li, and Y.-N. Wang, "Equivalent circuit effects on mode transitions in H₂ inductively coupled plasmas," *Phys. Plasmas* **22**, 043508 (2015).
- ¹⁵S. Mattei, K. Nishida, S. Mochizuki, A. Grudiev, J. Lettry, M. Q. Tran, and A. Hatayama, "Kinetic simulations and photometry measurements of the E-H transition in cylindrical inductively coupled plasmas," *Plasma Sources Sci. Technol.* **25**, 065001 (2016).
- ¹⁶T. Wegner, C. Küllig, and J. Meichsner, "On the E-H transition in inductively coupled radio frequency oxygen plasmas: I. density and temperature of electrons, ground state and singlet metastable molecular oxygen," *Plasma Sources Sci. Technol.* **26**, 025006 (2017).
- ¹⁷M. Schaeckens, N. R. Rueger, J. J. Beulens, X. Li, T. E. F. M. Standaert, P. J. Matsuo, and G. S. Oehrlein, "Effect of capacitive coupling on inductively coupled fluorocarbon plasma processing," *J. Vac. Sci. Technol. A* **17**, 3272–3280 (1999).
- ¹⁸H. Sugai, K. Nakamura, and K. Suzuki, "Electrostatic coupling of antenna and the shielding effect in inductive rf plasmas," *Jpn. J. Appl. Phys.* **33**, 2189–2193 (1994).
- ¹⁹K. Yoshida, H. Miyamoto, E. Ikawa, and Y. Murao, "Gate electrode etching using a transformer coupled plasma," *Jpn. J. Appl. Phys.* **34**, 2089–2094 (1995).
- ²⁰J.-H. Kim, H.-J. Lee, Y.-T. Kim, K.-W. Whang, and J.-H. Joo, "Effects of the axial external magnetic field on the reduction of the dielectric window damage due to capacitive coupling in the inductively coupled plasma," *J. Vac. Sci. Technol. A* **15**, 564–567 (1997).
- ²¹Y. J. Lee, K. N. Kim, G. Y. Yeom, and M. A. Lieberman, "Reduction of the electrostatic coupling in a large-area internal inductively coupled plasma source using a multicusp magnetic field," *Appl. Phys. Lett.* **85**, 1677–1679 (2004).
- ²²D. S. Lee, Y. K. Lee, and H. Y. Chang, "Characteristics of an inductively coupled plasma source using a parallel resonance antenna," *Plasma Sources Sci. Technol.* **13**, 701–706 (2004).
- ²³K. Takenaka, Y. Setsuhara, K. Nishisaka, A. Ebe, S. Sugiura, K. Takahashi, and K. Ono, "Characterization of inductively-coupled RF plasma sources with multiple low-inductance antenna units," *Jpn. J. Appl. Phys.* **45**, 8046–8049 (2006).
- ²⁴K. Suzuki, K. Konishi, K. Nakamura, and H. Sugai, "Effects of capacitance termination of the internal antenna in inductively coupled plasma," *Plasma Sources Sci. Technol.* **9**, 199–204 (2000).
- ²⁵J. Kim, H. Lee, D. Lee, and J. Lee, "The effects of capacitor termination at an internal icp antenna on the power coupling, plasma parameters and impurity incorporation," *Surf. Coatings Technol.* **21**, 5442–5445 (2007).
- ²⁶G. H. Gweon, J. H. Lim, S. P. Hong, and G. Y. Yeom, "Effect of capacitor installed in series with a ferrite-enhanced internal linear-type antenna on the properties of an inductively coupled plasma," *IEEE Trans. Plasma Sci.* **38**, 1499–1504 (2010).
- ²⁷D. Han, H.-C. Lee, H. J. Kim, Y. S. Kim, C.-W. Chung, and H. Chae, "Effects of capacitor termination to an antenna coil on the plasma parameters in a radio frequency inductively coupled plasma," *Plasma Sources Sci. Technol.* **22**, 055011 (2013).
- ²⁸J.-H. Moon, K.-H. Kim, M.-C. Lin, and C.-W. Chung, "Effects of antenna coil turns on plasma density and antenna voltage in solenoidal inductively coupled plasmas," *Phys. Plasmas* **23**, 113504 (2016).
- ²⁹R. A. Stewart, P. Vitello, D. B. Graves, E. F. Jaeger, and L. A. Berry, "Plasma uniformity in high-density inductively coupled plasma tools," *Plasma Sources Sci. Technol.* **4**, 36–46 (1995).
- ³⁰K. Bera, B. Farouk, and P. Vitello, "Inductively coupled radio frequency methane plasma simulation," *J. Phys. D Appl. Phys.* **34**, 1479–1490 (2001).
- ³¹I. M. El-Fayoumi and I. R. Jones, "The electromagnetic basis of the transformer model for an inductively coupled RF plasma source," *Plasma Sources Sci. Technol.* **7**, 179–185 (1998).
- ³²I. M. El-Fayoumi and I. R. Jones, "Theoretical and experimental investigations of the electromagnetic field within a planar coil, inductively coupled RF plasma source," *Plasma Sources Sci. Technol.* **7**, 162–178 (1998).
- ³³E. Kawamura, D. B. Graves, and M. A. Lieberman, "Fast 2D hybrid fluid-analytical simulation of inductive/capacitive discharges," *Plasma Sources Sci. Technol.* **20**, 035009 (2011).
- ³⁴H. Ellis, R. Pai, E. McDaniel, E. Mason, and L. Viehland, "Transport properties of gaseous ions over a wide energy range," *At. Data Nucl. Data Tables* **17**, 177–210 (1976).
- ³⁵A. V. Phelps, "Cross sections and swarm coefficients for nitrogen ions and neutrals in N₂ and argon ions and neutrals in Ar for energies from 0.1 eV to 10 KeV," *J. Phys. Chem. Ref. Data* **20**, 557–573 (1991).
- ³⁶J. T. Gudmundsson and E. G. Thorsteinsson, "Oxygen discharges diluted with argon: Dissociation processes," *Plasma Sources Sci. Technol.* **16**, 399–412 (2007).
- ³⁷M.-H. Lee and C.-W. Chung, "Self-consistent global model with multi-step ionizations in inductively coupled plasmas," *Phys. Plasmas* **12**, 073501 (2005).
- ³⁸S. Ashida, C. Lee, and M. A. Lieberman, "Spatially averaged (global) model of time modulated high density argon plasmas," *J. Vac. Sci. Technol. A* **13**, 2498–2507 (1995).

³⁹F. Kannari, M. Obara, and T. Fujioka, “An advanced kinetic model of electron-beam-excited KrF lasers including the vibrational relaxation in KrF*(B) and collisional mixing of KrF*(B,C),” *J. Appl. Phys.* **57**, 4309–4322 (1985).

⁴⁰V. Georgieva, A. Berthelot, T. Silva, S. Kolev, W. Graef, N. Britun, G. Chen, J. van der Mullen, T. Godfroid, D. Mihailova, J. van Dijk, R. Snyders, A. Bogaerts, and M.-P. Delplancke-Ogletree, “Understanding microwave surface-wave sustained plasmas at intermediate pressure by 2D modeling and experiments,” *Plasma Processes Polym.* **14**, 1600185 (2016).

⁴¹S. S. Todorov and E. R. Fossum, “Sputtering of silicon dioxide near threshold,” *Appl. Phys. Lett.* **52**, 365–367 (1988).

⁴²M. P. Seah and T. S. Nunney, “Sputtering yields of compounds using argon ions,” *J. Phys. D Appl. Phys.* **43**, 253001 (2010).

⁴³V. A. Godyak, R. B. Piejak, and B. M. Alexandrovich, “Electron energy distribution function measurements and plasma parameters in inductively coupled argon plasma,” *Plasma Sources Sci. Technol.* **11**, 525–543 (2002).